Surface Structure in an Accretion Disk Annulus with Comparable Radiation and Gas Pressure

Omer Blaes

Department of Physics, University of California, Santa Barbara, Santa Barbara CA 93106

Shigenobu Hirose

The Earth Simulator Center, JAMSTEC, Yokohama, Kanagawa 236-0001, Japan

and

Julian H. Krolik

Department of Physics and Astronomy, Johns Hopkins University, Baltimore, MD 21218

ABSTRACT

We have employed a 3-d energy-conserving radiation MHD code to simulate the vertical structure and thermodynamics of a shearing box whose parameters were chosen so that the radiation and gas pressures would be comparable. The upper layers of this disk segment are magnetically-dominated, creating conditions appropriate for both photon bubble and Parker instabilities. We find little evidence for photon bubbles, even though the simulation has enough spatial resolution to see them and their predicted growth rates are high. On the other hand, there is strong evidence for Parker instabilities, and they appear to dominate the evolution of the magnetically supported surface layers. The disk photosphere is complex, with large density inhomogeneities at both the scattering and effective (thermalization) photospheres of the evolving horizontally-averaged structure. Both the dominant magnetic support and the inhomogeneities are likely to have strong effects on the spectrum and polarization of thermal photons emerging from the disk atmosphere. The inhomogeneities are also large enough to affect models of reflection spectra from the atmospheres of accretion disks.

Subject headings: accretion, accretion disks — instabilities — MHD — radiative transfer

1.   Introduction

The first attempts to understand accretion disks concentrated on deriving radial profiles of azimuthally-averaged and vertically-integrated quantities in time-steady disks. For example, Shakura & Sunyaev (1973) and Novikov & Thorne (1973) worked out the theory for such disks around black holes by applying the constraints of energy and angular momentum conservation. When Shakura & Sunyaev (1973) introduced the notion that the stress responsible for moving matter inward through a disk should be proportional to the pressure, it was with a view toward tying the stress to local conditions in an azimuthally-averaged and vertically-integrated sense. Efforts were made within that framework to compute the actual vertical thickness as a function of radius, but it was recognized that this computation was subject to considerable uncertainty due to lack of knowledge of internal disk dynamics.

Particularly with the recognition that disk stresses can largely be explained by correlated MHD turbulence stirred by the magneto-rotational instability (as reviewed, for example, in Balbus & Hawley 1998), recently attention has been given to what may happen inside disks, even when their vertical scale-heights are quite small compared to the distance to the central object. This attention has included both analytic work on wave modes and instabilities that may exist (e.g. Nowak & Wagoner 1993; Gammie 1998; Kim & Ostriker 2000; Pessah & Psaltis 2005) and numerical simulations of vertically stratified shearing-box segments of disks (Brandenburg et al. 1995; Stone et al. 1996; Miller & Stone 2000; Turner 2004; Hirose, Krolik, & Stone 2006).

Special problems arise in understanding the vertical structure of disks when radiation pressure is comparable to or greater than gas pressure. As first pointed out by Shakura & Sunyaev (1973), this condition is likely to occur in the inner portions of disks accreting at more than a small fraction of Eddington, particularly when the central mass is $\gg 1 M_\odot$. Perhaps the biggest potential problem is that thermal and viscous instabilities in the vertically-integrated quantities might occur as a result of radiation pressure dominance (Lightman & Eardley 1974; Shakura & Sunyaev 1976).

The large radiation pressure regime may also be vulnerable to smaller scale photon bubble instabilities (Gammie 1998). The most rapidly-growing form of this instability occurs at short wavelengths, where photons diffuse rapidly, resulting in radiative amplification of magnetosonic waves (Blaes & Socrates 2003). At least for strong magnetic fields, the initial nonlinear evolution of the instability in this short wavelength limit produces trains of shocks (Begelman 2001; Turner et al. 2005). Begelman (2002, 2006) has suggested that these shock trains would permit accreting black holes to radiate at luminosities 1-2 orders of magnitude larger than Eddington.

We are embarked on a program to explore the nature of the internal dynamics in disks at varying levels of relative importance of radiation pressure support. We do this by conducting detailed numerical simulations that both conserve energy to high accuracy and include radiation transport in a vertically stratified disk annulus. The first such simulation was performed by Turner (2004) with a high ratio of radiation to gas pressure at the midplane. While very interesting results were obtained, the simulation achieved only partial energy conservation and was not able to reach low enough densities to incorporate the photosphere within the simulation domain. Solutions to these problems have since been found and a simulation of a disk annulus in which the radiation pressure was about 20% of the gas pressure was presented by Hirose, Krolik, & Stone (2006). In a companion paper to this one (Krolik et al. 2007), we report on the thermodynamic properties of a simulated disk annulus in which the time-averaged radiation and gas pressures were roughly equal.

In this paper, we investigate internal structures near the surface of the same disk annulus whose thermodynamics were studied in the companion paper. We concentrate on these upper regions because the shorter length scale instabilities predicted by linear theory tend to have their fastest growth rates there. As we shall show, two are of special interest: the photon bubble instability and the Parker instability. In addition, it is the structure of these surface layers that is most important in determining the degree to which the photon spectrum emerging from the disk deviates from a black body at the local effective temperature.

This paper is organized as follows. In section 2 we briefly summarize the methods and parameters of the simulation we are investigating. Then in section 3 we describe the properties of photon bubble and Parker instabilities that we expect based on applying linear instability theory to the horizontally averaged structure in the simulation. In section 4 we compare these expectations to what we actually observe in the three-dimensional structure of the simulation. Strong inhomogeneities are observed near the photosphere in the simulation, both in density and, to a lesser extent, temperature, and we describe these in section 5. In section 6, we discuss the possible implications of our results for models of the emergent and reflected photon spectra, and for the emergent photon polarization. Finally, we summarize our results in section 7.

2. Calculational Method

Our results are based on a 3-d radiation MHD simulation of a vertically stratified section of an accretion disk, computed under the shearing-box approximation. The code is described in greater detail in Hirose, Krolik, & Stone (2006), although the version we used differs slightly from that one by certain technical improvements. In its essential elements, this code

computes the equations of 3-d ideal MHD, capturing all grid-scale numerical dissipation as heat. Radiation transport and radiation forces are included, but with thermally-averaged opacity and emissivity and in the flux-limited diffusion approximation. Further details about initial conditions and boundary conditions are given in the companion paper (Krolik et al. 2007), which concentrates on describing the thermodynamics and larger-scale properties of this simulation.

In order to arrive at a disk annulus in which the radiation and gas pressures are comparable, we chose the following parameters for this shearing-box segment: The central mass is $6.62M_\odot$, the radius is $r = 150r_g = 1.5 \times 10^8$ cm, and the surface density is 4.7×10^4 g cm^{-2}. If it were described by a Shakura-Sunyaev stress ratio $\alpha = 0.02$, the mass accretion rate would produce a luminosity $0.1L_E$ if the efficiency were 0.1. The local effective temperature would then be 9.0×10^5 K. Our unit of length $H = 3.1 \times 10^6$ cm is the (half)-disk thickness in the gas-dominated limit, as given in Krolik (1999). The midplane optical depth is $(1.58 \pm 0.01) \times 10^4$, varying slightly due to the temperature-dependence of the free-free contribution. At all times, the opacity is dominated by Thomson scattering. The initial magnetic field is a twisted azimuthal flux tube with no net poloidal flux and energy density 1/25 the midplane gas plus radiation pressure.

Our computational box had a vertical thickness of $12H$, stretching symmetrically above and below the midplane. Its radial thickness was $(3/4)H$ and its azimuthal thickness was $3H$. These dimensions were described by $512 \times 32 \times 64$ cells, respectively. The simulation ran for 318 orbits, equivalent to more than 40 thermal times. As discussed in the companion paper (Krolik et al. 2007), the epoch with highest total energy content was at 90 orbits, and the epoch with lowest total energy content was at 150 orbits. We focus our analysis in this paper on just these two epochs.

3. Expectations Based on Linear Instability Theory

3.1. Photon bubbles

To check for the presence of photon bubble instabilities in the present simulation, we must first delineate the regions where photons diffuse rapidly relative to the time scales relevant for acoustic waves in a gas and radiation mixture (Agol & Krolik 1998). When gas and radiation exchange heat rapidly, an excellent approximation for most, but not all, regimes of plasma acoustic behavior in the case under consideration here, it is convenient to write the dispersion relation for compressive waves in terms of an effective sound speed (e.g.

Appendix B of Blaes & Socrates 2003)

$$C_s^2 = \frac{\omega\left[e + 4E\right]c_t^2 + \frac{ick^2}{3\kappa_F\rho}4Ec_i^2}{\omega\left[e + 4E\right] + \frac{ick^2}{3\kappa_F\rho}4E}.$$

(1)

Here $k = 2\pi/\lambda$ is the wavenumber of the disturbance, $\omega = kC_s$ is the corresponding angular frequency, e is the internal energy density of the gas, E is the radiation energy density, ρ is the density, and κ_F is the flux mean opacity. The quantity $c_i = (p_g/\rho)^{1/2}$ is the isothermal sound speed in the gas, where p_g is the gas pressure. The total adiabatic sound speed c_t of the fluid is defined by

$$c_t^2 = \frac{16E^2 + 60(\gamma - 1)Ee + 9\gamma(\gamma - 1)e^2}{9(e + 4E)\rho} = \frac{\Gamma_1(p_g + E/3)}{\rho},$$

(2)

where $\gamma = 5/3$ is the adiabatic index of the gas and Γ_1 is the first generalized adiabatic exponent relating pressure and volume changes when radiation and matter are tightly thermally coupled (Chandrasekhar 1967). Equation (1) shows that the wave speed ranges from c_i to c_t; the frequency for a given wavelength may therefore be easily bounded.

It is then straightforward to show that acoustic disturbances with wavelengths satisfying

$$\lambda < \frac{2\pi c}{3\kappa_F\rho c_i}\left(\frac{4E}{e + 4E}\right)\left(\frac{c_i}{c_t}\right)^2 \equiv \lambda_R$$

(3)

are in a regime where photons diffuse rapidly compared to the wave period. As a result, the radiation pressure response is lost, and the sound speed approaches the isothermal sound speed in the gas c_i. On the other hand, acoustic disturbances with longer wavelengths satisfying

$$\lambda > \lambda_S \equiv \frac{c_t}{c_i}\lambda_R = \left[\Gamma_1\left(1 + \frac{E}{3p_g}\right)\right]^{1/2}\lambda_R$$

(4)

trap photons, and therefore propagate at c_t, the total sound speed in the gas and radiation. For intermediate wavelengths with $\lambda_R < \lambda < \lambda_S$, the damping of the disturbances is maximal. However, when the radiation energy density is not much larger than the gas pressure, as in the present simulation, the maximal damping rate is less than the mode period, and $c_t \sim c_i$.

Fig. 1 shows the critical wavelengths λ_R and λ_S as a function of height at the highest (90 orbits) and lowest (150 orbits) total energy epochs in the simulation, based on horizontally averaged data. Also indicated is the range of wavelengths in the azimuthal direction that can be resolved by the code, from eight azimuthal cell sizes to the box size in the azimuthal direction. Near the midplane, photons are trapped at all epochs for acoustic disturbances at all wavelengths resolved by the code. Outside $\pm 2.5H$, compressive disturbances are in

the rapid diffusion limit for all accessible wavelengths at $t = 150$ orbits, when the disk is relatively cool. Even at $t = 90$ orbits, when the disk is relatively hot, there is a factor of two range of resolved wavelengths that are in the rapid diffusion limit in the subphotosphere surface layers.

In addition to the rapidity of photon diffusion, another issue of relevance to photon bubbles is how rapidly gas and radiation exchange heat. As discussed in Blaes & Socrates (2003), the gas and radiation temperatures are effectively locked together in a rapidly growing photon bubble disturbance provided $\omega_{\mathrm{th}} \equiv 4E\kappa\rho c/e$ is greater than the gas acoustic frequency g/c_i associated with a gas pressure scale height. (Here κ is the Planck mean opacity associated with the free-free absorption used in the code.) The ratio of these two rates is shown in Fig. 2, and except for the uppermost layers at 150 orbits, rapid heat exchange is a good approximation for photon bubbles.

In this thermally locked, rapid diffusion regime, photon bubbles reach their maximum growth rates γ_d over a finite range of wavelengths. The approximate lower bound is a short thermal "cutoff wavelength" $\lambda_{\mathrm{cutoff}} = 2\pi c_i/(\omega_{\mathrm{th}}\gamma_d)^{1/2}$ below which rapid heat exchange fails to be a good approximation in the amplifying acoustic wave, and the wave stabilizes due to the damping associated with the slow heat exchange. The approximate upper bound is a long "turnover wavelength" $\lambda_{\mathrm{turnover}} = \gamma_d/v_{\mathrm{ph}}$ above which the wave is no longer a simple magnetosonic wave propagating with phase speed v_{ph}, and the growth rate declines. These wavelength bounds are shown in Fig. 3 for the horizontally-averaged conditions in the simulation.

Fig. 4 shows the expected maximum growth rate γ_d of the photon bubble instability (Eq. 93 of Blaes & Socrates 2003) as a function of height in the simulation box at 90 and 150 orbits. We assumed that the relevant wavelengths are in the rapid diffusion limit, which Figs. 1 and 3 show to be valid at least in the subphotospheric surface layers. We also assumed a purely azimuthal magnetic field and a wave vector orientation inclined upward at 45 degrees to the horizontal in the vertical/azimuthal plane. Much of the field is in fact in the azimuthal direction in the upper layers and 45 degrees is close to the inclination that gives maximal growth. Apart from particular cases where the growth rate strictly vanishes, other field orientations and wave vector directions alter the growth rates by geometric factors of order unity. It is important to note that we calculate growth rates only inside the Rosseland mean photosphere of the horizontally averaged structure, as the photon bubble instability does not exist when the medium is optically thin.

Figs. 3 and 4 show that at $t = 90$ orbits, modes with wavelengths shorter than about a scale height should grow by many e-foldings per orbital period in the surface layers beneath the Rosseland mean photosphere. Our simulation has plenty of resolution to see these rapid

growth rates: a scale height projected through 45° corresponds to 15 zones in the ϕ-direction and 30 zones in the z-direction. Resolution studies by Turner et al. (2005) found that the growth rates predicted by linear theory should be recovered in a numerical simulation to within ten percent provided there are more than 15 zones per wavelength. On the other hand, Fig. 3 also shows that wavelengths more than a factor of two smaller than the turnover wavelength are not well-resolved. Figs. 6 of Blaes & Socrates (2003) and 12 and 13 of Turner et al. (2005) show that the growth rate at the turnover wavelength can be smaller by as much as a factor of two compared to the maximum growth rate γ_d, but that still gives $4 - 5$ e-foldings per orbital period. The maximum growth rates are considerably smaller at $t = 150$ orbits, and will be reduced further above $z = 2.5H$ in the upper half of the simulation due to the breakdown in good thermal coupling between the gas and radiation. Photon bubbles are therefore most likely to be present at $t = 90$ orbits.

3.2. The Parker instability

All analyses of the magnetosonic photon bubble instability so far have assumed a uniform magnetic field in the equilibrium (Gammie 1998; Begelman 2001; Blaes & Socrates 2003). Even if that field is strong, it does not support the background against gravity. In contrast, we have shown in section §3.2 of the companion paper (Krolik et al. 2007) that the magnetic field in our simulation provides the dominant support against gravity at high altitudes. This fact immediately suggests that the Parker instability (Parker 1966, 1967) might play a role instead of or in addition to the photon bubble instability.

We can get a rough idea of the relevance of the Parker instability to this simulation by examining its dispersion relation in an isothermal atmosphere. We do this in the Appendix. Figs. 5 and 6 show the maximum growth rate [equation (A16)] and characteristic wavelengths [equations (A14)-(A15)] of the Parker instability as a function of height at $t = 90$ and 150 orbits. These figures are based on horizontally averaged data at each epoch, and on the assumption that the magnetic field is azimuthal. We also assumed that radiative diffusion is rapid, so that perturbations in the gas are isothermal, though we believe that the results are approximately valid even under conditions where the radiation is trapped. This is because the Parker instability arises from a competition between magnetic pressure and thermal pressure, and the gas and radiation pressures are comparable here. Fig. 6 leads us to expect that the regions outside approximately $\pm 2H$ will be Parker unstable during the high total energy epoch at $t = 90$ orbits. In the low total energy epoch at $t = 150$ orbits, we expect the regions $z < -2H$ and $H < z < 3H$ to be Parker unstable.

The Parker instability growth rates exceed the orbital frequency by roughly a factor of

two, and are larger than the maximal photon bubble growth rates except perhaps very near the Rosseland mean photosphere at $t = 90$ orbits. Interestingly, the wavelength for maximal growth of the Parker instability roughly corresponds to the azimuthal size of the box, and our analysis in the Appendix indicates that the corresponding wave vector should be in the horizontal direction.

4. To what extent are instabilities present in the simulation?

4.1. Photon bubbles

The simulation results are somewhat ambiguous as to the presence of the photon bubble instability. Fig. 7 shows the density, magnetic field, and velocity field in the vicinity of the upper photosphere at 90 orbits, the time of highest total energy in the simulation. Two photospheres are actually indicated in this figure, both calculated from the horizontally averaged structure at this epoch: the Rosseland mean photosphere and the effective, or thermalization photosphere. The latter is the outermost surface where photons exchange energy with matter. It is therefore the surface inside of which photons can come into thermal equilibrium with the matter. Because Thomson scattering dominates the free-free absorption opacity throughout the domain of the simulation, the effective photosphere is significantly deeper than the Rosseland mean photosphere.

In the region $3H < z < 4H$ there are 2-3 relatively high density regions which are somewhat reminiscent of the shock trains that form in the initial nonlinear development of the photon bubble instability (Begelman 2001; Turner et al. 2005). The high density streak stretching diagonally from the upper left $(-0.5H, 3.8H)$ to the lower right $(0.7H, 3.2H)$ in the center of the figure is almost certainly a shock, as the velocity field has significant convergence in this region. Two other shock-like features in the lower left of the figure [ranging from $(-0.9H, 3.2H)$ to $(-0.5H, 3.0H)$ and from $(-1.1H, 3.1H)$ to $(-0.7H, 2.8H)$] run parallel to the first shock, although whether these are true shocks is not completely clear as the velocity field does not show as much convergence as at the first shock. The magnetic field lines show a fairly discontinuous change in orientation across the first shock, which might be indicative of some buckling under the weight of the dense material. There is also a rapid change in orientation of the magnetic field lines near the other two putative shocks. Examination of nearby radial slices at the same time shows that the first shock extends over only $\simeq 0.2H$ in radius. Our simulation data dumps lack the time resolution to explore its evolution: it is absent and the overall structure is quite different one orbit earlier and one orbit later. This is not surprising, however, as the background differential rotation will shear out a region of radial thickness $x = 0.2H$ to extend over $3\pi x \simeq 2H$ in the azimuthal

direction after one orbit.

It is unclear whether these shocks are the result of photon bubble instability. To try to resolve this ambiguity, we have investigated how the radiation flux and fluid velocity are correlated in the layers where the photon bubble instability is expected. At least in the rapid diffusion limit of interest here, photon bubbles are fundamentally a radiative amplification of a magnetosonic wave. The density compressions and rarefactions in the wave alter the diffusion paths of photons in such a way as to produce radiation flux perturbations that everywhere make acute angles with the fluid velocities in the wave (Turner et al. 2005). Oscillating radiation pressure forces in phase with the oscillating fluid velocities are the result, which drive the wave to larger amplitudes. To check for this distinctive directional relationship between the perturbed forces and velocities, we show in Fig. 8 the distribution of cosines of the angle θ between the fluctuating radiation flux and fluid velocity vectors at all grid points in a set of horizontal slices through the simulation at 90 orbits. To be precise,

$$\cos\theta = \frac{(\mathbf{F}- < F_z > \hat{\mathbf{z}}) \cdot (\mathbf{v} + \frac{3}{2}\Omega x \hat{\mathbf{y}})}{|\mathbf{F}- < F_z > \hat{\mathbf{z}}||\mathbf{v} + \frac{3}{2}\Omega x \hat{\mathbf{y}}|}, \tag{5}$$

where the angle brackets refer to a horizontal average at the particular height in question. We subtract off the horizontal average of the vertical flux component because a radiation driven outflow would also give rise to a correlation between flux and velocity without having anything to do with photon bubbles.

As can be seen in Fig. 8, at three of the four sample heights, there is essentially no directional correlation between the fluctuating part of the radiation flux and the fluid velocity. Only at $z = +2.4H$ is there a significant positive correlation; in fact, there is a weak anti-correlation at $z = +3.3H$ and $3.8H$. Ironically, our application of the linear theory of photon bubbles to these data suggests that they grow only for $z > 2.5H$. We conclude, therefore, that there is little evidence for photon bubble-driven dynamics here.

4.2. Parker instability

Although evidence for photon bubbles is scant, evidence for Parker instability is strong. This mode involves an interplay between support against gravity provided by magnetic pressure forces and restraint against magnetic buoyancy provided by magnetic tension forces. We therefore begin this part of our analysis by mapping out the strengths of these forces.

The vertical accelerations produced by magnetic tension and magnetic pressure are

$$a_T = \frac{1}{4\pi\rho} \left(B_x \frac{\partial B_z}{\partial x} + B_y \frac{\partial B_z}{\partial y} \right) \tag{6}$$

and

$$a_P = \frac{-1}{8\pi\rho} \frac{\partial}{\partial z} \left(B_x^2 + B_y^2 \right), \tag{7}$$

respectively. These accelerations are plotted in Fig. 9. In a volume-averaged sense, the magnetic pressure force almost always pushes vertically outward; by contrast, in the same sense of averaging, the magnetic tension force generally holds matter in. In this volume-averaged sense, the two magnetic forces appear almost to balance each other. As we shall see shortly, in Parker modes there is a strong correlation between the sense of curvature of the magnetic field (which controls the direction of the tension force) and the gas density: relatively low density and inward tension force are often found together. For fixed total mass, low density regions must always occupy more total volume than those of high density, so inward magnetic tension regions dominate in a volume average. On the other hand, support against gravity is best thought of in terms of mass-weighted quantities (right-hand panel of Fig. 9). Averaged in this fashion, magnetic tension becomes much less important, and we see that the upper layers of the disk are, as previously noted, primarily supported by magnetic pressure gradients.

The fact that large inward magnetic tension forces begin outside $z = \pm 3H$ is an indication that the Parker instability is in operation at those altitudes. This height is not far from the $z = \pm 2H$ boundaries where we expected the Parker instability to develop on the basis of our simplified linear analysis.

A further diagnostic of Parker instability can be seen in the density and magnetic field structure shown in Fig. 7 at $t = 90$ orbits. The densest regions of gas lie in troughs of magnetic field lines, whereas the lighter regions are located near magnetic field line crests. To quantitatively check this visual impression, the left hand panel of Fig. 10 shows the magnetic tension force per unit volume versus the density at each grid zone in a $z = 2.75H$ horizontal slice through the box at this epoch. There is a clear correlation between these two quantities: gas heavier (lighter) than average is predominantly associated with upward (downward) tension forces.

Fig. 11 shows the upper surface layers at $t = 150$ orbits. The structure above the photosphere is very complex with large flow velocities, and the $\phi - z$ projection of the field shows circulation, including regions of nearly vertical field lines. This complex structure is no doubt related to the large deviations from hydrostatic balance (see right panel of Fig. 6 in the companion paper, Krolik et al. 2007). Nevertheless, a long wavelength Parker mode appears to be present in the region $2H < z < 3H$, which is again where it was expected to occur based on the minimum unstable wavelength shown in Fig. 6. Its wavelength and horizontal orientation also conform with the linear analysis expectations. The right hand panel of Fig. 10 shows that tension is again highly correlated with density in the $z = 2H$

horizontal slice.

This correlation between density and tension forces is perhaps the strongest evidence that Parker modes play a significant role in the outer layers of the simulation. A volumetric rendering of the correlation is shown in Fig. 12. Regions that are denser than average at a given height are mostly associated with field line valleys, whereas low density regions are mostly associated with crests in the field lines.

Fig. 13 shows the fractional horizontal surface area at each height for which the correlation between density and tension forces holds. Within approximately two scale heights on either side of the midplane, there is no correlation. Outward and inward tension forces in this region are equally likely to be associated with higher and lower than average densities, so the fractional surface area exhibiting the expected behavior of the Parker instability is fifty percent. Further away from the midplane at $t = 90$ orbits, however, the vertically outward (inward) tension forces are more likely to be associated with lower (higher) than average density, as expected from the Parker instability. This vertical dependence of the magnetic tension-density correlation is completely consistent with our linear instability expectations from section 3.2 above: unstable growth at $|z| \gtrsim 2H$ and no instability closer to the midplane. The situation is approximately the same at $t = 150$ orbits, except that there is no evidence of the expected Parker correlation below $z \simeq -3H$, or near $z = 3H, 4H$, and above $5H$. Our linear analysis of section 3.2 predicted that at this epoch the regions $z < -2H$ and $H < z < 3H$ would be Parker unstable. Again, we suspect that the discrepancy arises partly from the breakdown of hydrostatic equilibrium in the outer layers at this epoch, as shown in the right panel of Fig. 6 of the companion paper.

It is fortunate that our simulation domain just happened to be the right size for the maximal Parker instability wavelengths to fit inside the box. Whether these modes can fit in the computational domain is clearly something to be borne in mind when choosing parameters for future stratified shearing box simulations. It is unclear whether the finite azimuthal extent of the box might be affecting the nonlinear saturated state of the instability. One could imagine, for example, that the tension forces could be reduced if the nonlinear development of the instability cascaded toward longer wavelengths, but this would not be possible in our finite shearing box. Clearly further work with larger simulation domains is warranted in the future.

For comparison, the upper surface layers in the middle of the box near the end of the gas pressure dominated simulation of Hirose, Krolik, & Stone (2006) are shown in Fig. 14. The structure in the lower regions of this figure again appears to be consistent with the Parker instability. Fig. 15 shows that the expected correlation between density and tension forces is again widespread outside approximately two scale heights away from the midplane. Not

surprisingly, the Parker instability appears to be generically important in the magnetically supported upper layers of accretion disks even when there is little radiation pressure.

5. Photospheric Irregularity

Very large, irregular density inhomogeneities are evident in the surface layers and extend as deep as the effective photosphere of the horizontally-averaged structure at all epochs. The distribution of densities at the upper effective and Rosseland mean photospheres at 90 and 150 orbits is shown in Fig. 16. The density fluctuations range over factors of approximately ten above and below the mean, with small isolated rarefied regions that are even less dense still. The vertical distribution of horizontally-averaged root mean square fractional fluctuation of density is shown in Fig. 17 for the same epochs. The large density inhomogeneities clearly extend over a broad range of heights outside $\pm 2H$.

One possible explanation for the presence of these density inhomogeneities lies in the fact that, in isolated parts of the most rarefied regions outside the effective photosphere, the gas temperature can greatly exceed (by greater than a factor 100) the effective temperature of the radiation, as shown in Figs. 18 and 19. The code assumes that gas and radiation exchange heat purely through free-free absorption and emission, and the density is so low in these regions that the gas and radiation are unable to equilibrate through this channel. Including Compton scattering in the gas and radiation energy equations would enhance the thermal coupling. The ratio of time scales of Compton to free-free cooling of the gas is approximately

$$\frac{t_{\mathrm{Comp}}}{t_{ff}} \simeq \frac{\kappa(T_{\mathrm{gas}}^4 - T_{\mathrm{rad}}^4)m_e c^2}{4k_{\mathrm{B}}(T_{\mathrm{gas}} - T_{\mathrm{rad}})\kappa_T T_{\mathrm{rad}}^4}, \tag{8}$$

where κ is the Planck mean free-free opacity, κ_T is the Thomson opacity, T_{gas} is the gas temperature, and T_{rad} is the effective temperature of the radiation. In the conditions of the current simulation, free-free is faster than Compton in exchanging heat between the gas and radiation throughout most of the volume. However, in the isolated regions where the gas temperature significantly exceeds the radiation temperature, the Compton cooling time can be shorter than the free-free cooling time by factors of 5 to 10. The gas may therefore be artificially too hot in these regions, because we did not include Compton cooling in the simulation. Artificially elevated temperature might enhance the degree of inhomogeneity by artificially raising the gas pressure. Although this effect may explain the regions we see where the gas and radiation temperatures are far apart, it cannot explain all regions of large density inhomogeneity: Figs. 18 and 19 show that the radiation and gas temperatures are equal at the effective photosphere (as they must be), and yet there can be large density

contrasts there.

Photon bubbles would produce inhomogeneities, but we have failed to find any other evidence for these instabilities in the simulation. Moreover, substantial inhomogeneities persist even in the optically thin uppermost regions, where the photon bubble instability cannot act. Figs. 16 and 17 show that strong density inhomogeneities are also present in the gas pressure dominated simulation of Hirose, Krolik, & Stone (2006). Photon bubbles are almost certainly irrelevant in this case, and therefore cannot be responsible for the inhomogeneities that are seen.

As noted by Hirose, Krolik, & Stone (2006), a more likely explanation for the inhomogeneities is that they are a result of the fact that magnetic forces dominate gas and radiation pressure in these layers. Because density only affects gas pressure gradients, and these generally play only a small role in the dynamics in these regions, it is not surprising that density inhomogeneities develop in response to fluctuating magnetic forces.

6. Implications for Emergent and Reflected Photons

Our earlier result that magnetic support extends the upper atmospheres of accretion disks when gas pressure dominates (Hirose, Krolik, & Stone 2006) now appears to apply to conditions in which radiation pressure is comparable to gas pressure. This additional source of support against gravity creates a lower density photosphere than would otherwise be found. As a result, electron scattering is enhanced over absorption, and the matter's ionization balance shifts toward more highly-ionized species, weakening absorption edges and strengthening emission edges. Both of these effects generically lead to a *hardening* of the emergent spectrum (Blaes et al. 2006). On the basis of the calculations reported here, we expect that magnetically supported, extended atmospheres should continue to exist in rings even where radiation and gas pressure are comparable.

However, we also see strong, irregular density inhomogeneities in the surface layers beneath the scattering photosphere, and these inhomogeneities were also present in the gas pressure dominated simulation (Figs. 14-17). The effect of strong inhomogeneities on the emergent spectrum has been investigated in the ordered shock train geometry produced in the initial nonlinear development of the photon bubble instability (Davis et al. 2004; Begelman 2006). At least in this geometry, and at least provided thermal absorption/emission dominates Compton scattering in the energy exchange between radiation and matter, the high density regions enhance the thermalization of radiation with matter. This typically produces a *softening* of the spectrum compared to what would emerge from an atmosphere which is a

horizontal average of the medium. It remains to be seen which of these two opposing effects on the spectrum, softening by inhomogeneities vs. hardening by magnetic support, will be dominant, and how much effect Compton scattering can have in those regions where the gas temperature rises well above the radiation temperature.

The very inhomogeneous and irregular nature of the photosphere is also likely to reduce the degree of polarization of the emitted photons from a scattering dominated atmosphere, as it breaks the plane parallel symmetry. These inhomogeneities represent a physical realization of the "rough surface" proposed and investigated by Coleman & Shields (1990) in the context of continuum polarization from active galactic nuclei. As first suggested by Gnedin & Silant'ev (1978), Faraday depolarization may also be significant. The estimated rotation angle at the peak wavelength of a thermal spectrum [i.e., the peak of $B_\lambda(T)$] is $\simeq 0.8\tau_T R^{1/2}$ radians. Here τ_T is the Thomson optical depth to the surface where the underlying polarization is imprinted; we expect that because the opacity in these disk atmospheres is primarily Thomson scattering, $\tau_T \simeq 1$. The Faraday rotation is also proportional to R, the ratio of magnetic pressure to radiation pressure, if we suppose that the component of the field along the line of sight is a fixed and substantial fraction of the total. Using horizontal averages of the pressures, the highest total energy epoch in the current simulation ($t = 90$ orbits) has $R \sim 7$ at the lower photosphere and $R \sim 3.5$ at the upper photosphere. In both, the rotation angle is then ~ 2 radians per unit Thomson depth, large enough to give rise to significant Faraday depolarization.

Magnetic support of the surface layers could also have implications for X-ray reflection models that incorporate only gas and radiation pressure in the hydrostatic equilibrium (e.g. Nayakshin, Kazanas, & Kallman 2000). Most notably, the reduced density that follows from magnetic support will make photoionization relatively stronger. It is also unclear that the discontinuous, thermally stable structures that form in these models would exist if magnetic fields dominate the hydrostatic support. The right hand panel of Fig. 16 shows that large density inhomogeneities exist on the scale of a Thomson depth, and these may also affect the reflection spectrum. This effect has been explored in a preliminary fashion by Ballantyne, Turner & Blaes (2004) and Ballantyne, Turner, & Young (2005), who performed radiative transfer calculations through one dimensional inhomogeneous structures. Density variations of only a factor of a few were enough to produce significant changes in the reflection spectrum (Ballantyne, Turner & Blaes 2004), and we have more than that at the Rosseland mean ($\simeq$ Thomson) photosphere. Of course, the inhomogeneities themselves might be affected by heating by external radiation fields. This topic is clearly one that deserves further investigation.

7.   Summary

Hydrostatic equilibrium is often thought of in terms of a balance between gravity and any of three sorts of pressures: gas, radiation, and magnetic. However, we find that in the upper, magnetically-dominated layers of this disk segment, magnetic tension forces are almost as strong as magnetic pressure forces, at least in a volume-averaged sense. This is clearly because the nonlinear development of the transverse Parker instability is controlling the dynamics of the magnetic field in these upper layers. In a mass-averaged sense, however, magnetic pressure is still the dominant source of vertical support.

In contrast to the Parker instability, there is very little evidence for photon bubbles, even though their predicted linear growth rates are almost as large as the Parker growth rates, and the relevant unstable wavelengths are resolved.

Strong density inhomogeneities are present in the region between the effective (thermalization) and Rosseland mean ($\simeq$ scattering) photospheres. This was also true in the gas pressure dominated simulation of Hirose, Krolik, & Stone (2006), and these inhomogeneities are almost certainly the result of the large magnetic forces in the surface layers. Provided Compton scattering is less important than true absorption processes in thermally coupling photons with matter, these inhomogeneities are likely to enhance thermalization and therefore soften the emergent spectrum. This spectral softening mechanism may counteract to some extent the reduction in thermalization, and therefore the spectral hardening, caused by the lower average densities that are produced by magnetic support of the atmosphere. Inhomogeneities are likely to reduce the polarization of the emergent photons, and the magnetic fields in the atmosphere will reduce it still further through Faraday depolarization. Finally, the inhomogeneities we see at the scattering photosphere appear to be strong enough to affect X-ray reflection spectra.

More work needs to be done to elaborate on these conclusions. Given that the size of the linearly unstable Parker wavelengths is comparable to the azimuthal size of the box, it would be worthwhile in future to run simulations with larger azimuthal domains to see if this alters the magnetic equilibrium in the upper layers. Unfortunately, these simulations are expensive, so performing a full parameter survey is difficult.

It is not completely clear why we have failed to find evidence for photon bubbles in the present simulation. The accessible growing wavelengths are not too far below the turnover wavelength, and increasing the dynamic range of the simulation by decreasing the cell size would enable us to access even faster growing wavelengths which might then be better able to compete with the Parker instability. However, to fully understand which instability should dominate requires, at the very least, a linear instability analysis of an equilibrium with both

magnetic pressure support and a diffusive radiation flux. Such an equilibrium would then be more representative of the conditions we are finding in the simulation, and would be vulnerable to both the Parker and photon bubble instabilities. It could be that these two instabilities couple together in nontrivial ways, although their physical driving mechanisms are quite different. The transverse Parker instability turns a slow magnetosonic wave into an exponentially growing disturbance if magnetic pressure gradients are large enough. The fastest growing photon bubble instability is an overstability of, again, a slow magnetosonic wave, but is driven by the background radiation pressure.

Whether the emergent spectrum is harder due to magnetic support or softer due to density inhomogeneities when compared to plane parallel atmosphere models that neglect magnetic support will require a three dimensional radiative transfer calculation through the structures seen in the simulation. Monte Carlo calculations may be the way to approach this problem (e.g. Davis et al. 2004), and these could also include polarization with Faraday rotation (Agol & Blaes 1996). It might also be possible to calculate X-ray reflection in a similar fashion, though one would have to include the resulting photoionization self-consistently.

It remains to be seen what will happen when radiation pressure becomes dominant at the midplane. Photon bubbles should have even stronger growth rates in that regime, and may be more relevant. However, they will also be more difficult to resolve in a simulation because their characteristic wavelengths are only of order the gas pressure scale height. We expect to be able to report on simulations with large radiation pressure in the near future.

A. Appendix: Simplified Derivation of Parker Instability in a Radiating Medium

Assuming the gas and radiation are locked to the same temperature and that the medium is optically thick, the equations of radiation magnetohydrodynamics are

$$\frac{\partial \rho}{\partial t} + \nabla \cdot (\rho \mathbf{v}) = 0, \tag{A1}$$

$$\rho \left(\frac{\partial \mathbf{v}}{\partial t} + \mathbf{v} \cdot \nabla \mathbf{v} \right) = -\nabla p_{\mathrm{g}} + \rho \mathbf{g} + \frac{1}{4\pi} \mathbf{B} \cdot \nabla \mathbf{B} - \frac{1}{8\pi} \nabla B^2 + \frac{\kappa_{\mathrm{F}} \rho}{c} \mathbf{F}, \tag{A2}$$

$$\frac{\partial}{\partial t}(e + E) + \mathbf{v} \cdot \nabla(e + E) + \left(\gamma e + \frac{4}{3} E \right) \nabla \cdot \mathbf{v} = -\nabla \cdot \mathbf{F}, \tag{A3}$$

$$\mathbf{F} = -\frac{c}{3\kappa_{\mathrm{F}} \rho} \nabla E, \tag{A4}$$

and

$$\frac{\partial \mathbf{B}}{\partial t} = \nabla \times (\mathbf{v} \times \mathbf{B}), \tag{A5}$$

where

$$e = \frac{p_{\mathrm{g}}}{(\gamma - 1)}, \quad p_{\mathrm{g}} = \frac{\rho k_{\mathrm{B}} T}{\mu}, \quad \text{and} \quad E = aT^4. \tag{A6}$$

We adopt a simplified, static equilibrium structure in which the gravitational acceleration $\mathbf{g} = -g\hat{\mathbf{z}}$ is constant. Including the linear increase of g with height merely complicates the form of the unstable eigenfunctions and is not really justified here given the additional simplifications we are making. These include assuming that the background medium is isothermal and that the background magnetic energy density is proportional to the density. These assumptions imply that the isothermal sound speed in the gas c_{i} and the Alfvén speed v_{A} are constants, which greatly simplifies the analysis. A more serious consequence of these assumptions is that the background radiation flux $\mathbf{F}$ vanishes, and does not help support the medium against gravity. Because of this, we immediately lose the driving that causes photon bubbles. Nevertheless, we still hope to capture the basic growth rates and wavelength scales of the Parker instability in the magnetically dominated upper layers of our simulation. Finally, we assume that the background magnetic field is horizontal: $\mathbf{B} = B(z)\hat{\mathbf{y}}$.

With all these assumptions, hydrostatic equilibrium requires that the background density satisfies

$$\rho = \rho_0 \exp \left(-\frac{z}{H} \right), \tag{A7}$$

where

$$H = \frac{2c_{\mathrm{i}}^2 + v_{\mathrm{A}}^2}{2g}. \tag{A8}$$

Linearizing equations (A3) and (A4) about our background, and assuming that our disturbances are at short enough wavelengths that the rapid diffusion limit of equation (3) is satisfied immediately gives us $\delta T = 0$. Assuming the perturbations have a spacetime dependence of $f(z) \exp[i(k_x x + k_y y - \omega t)]$, and eliminating the magnetic field and pressure perturbations using the flux-freezing equation and equation of state, the linearized continuity and momentum equations become

$$-i\omega \frac{\delta\rho}{\rho} + ik_x \delta v_x + ik_y \delta v_y - \frac{\delta v_z}{H} + \frac{\partial \delta v_z}{\partial z} = 0, \tag{A9}$$

$$(\omega^2 - k_x^2 v_A^2 - k_y^2 v_A^2)\delta v_x - \frac{ik_x v_A^2}{2H}\delta v_z + ik_x v_A^2 \frac{\partial \delta v_z}{\partial z} - \omega k_x c_i^2 \frac{\delta \rho}{\rho} = 0, \tag{A10}$$

$$\omega^2 \delta v_y - \frac{ik_y v_A^2}{2H}\delta v_z - \omega k_y c_i^2 \frac{\delta \rho}{\rho} = 0, \tag{A11}$$

and

$$\left(\omega^2 - k_y^2 v_A^2 + \frac{v_A^2}{2H^2}\right)\delta v_z - \frac{3v_A^2}{2H}\frac{\partial \delta v_z}{\partial z} + v_A^2 \frac{\partial^2 \delta v_z}{\partial z^2} + \frac{i\omega v_A^2}{2H}\frac{\delta \rho}{\rho} + i\omega c_i^2 \frac{\partial}{\partial z}\left(\frac{\delta \rho}{\rho}\right) - \frac{ik_x v_A^2}{H}\delta v_x + ik_x v_A^2 \frac{\partial \delta v_x}{\partial z} = 0. \tag{A12}$$

We now adopt the *ansatz* that the z-dependence of the velocity perturbations and relative density perturbation is $\exp[ik_z z + z/(2H)]$, where k_z is a real number representing the wave vector in the vertical direction. The $\exp[z/(2H)]$ factor implies that $\rho|\delta v^2|$ is constant with height, thereby guaranteeing energy conservation for propagating waves (see e.g. section 53 of Mihalas & Mihalas 1984). We then obtain the dispersion relation

$$\omega^6 - \left[\left(k^2 + \frac{1}{4H^2}\right)(c_i^2 + v_A^2) + k_y^2 v_A^2\right]\omega^4 + v_A^2\left(2c_i^2 + v_A^2\right)\left(k_y^2 k^2 + \frac{k_x^2}{4H^2}\right)\omega^2$$
$$+ k_y^2 v_A^4\left[-k^2 k_y^2 c_i^2 + \frac{k_x^2}{4H^2}\left(2c_i^2 + v_A^2\right) + \frac{k_y^2}{4H^2}(c_i^2 + v_A^2)\right] = 0, \tag{A13}$$

where $k^2 \equiv (k_x^2 + k_y^2 + k_z^2)^{1/2}$ is the total wavenumber of the perturbation. Equation (A13) is identical to the original dispersion relation (I.19) of Parker (1967), restricted to isothermal perturbations.

Instability only exists if $k_y \neq 0$, and when it does, maximum growth occurs for horizontal wavenumbers ($k_z = 0$). In this case, instability occurs only for wavelengths $\lambda_y \equiv 2\pi/k_y$ satisfying

$$\lambda_y > \lambda_{\text{Parker}} \equiv \begin{cases} \frac{2\pi c_i(2c_i^2 + v_A^2)}{g(c_i^2 + v_A^2)^{1/2}} & \text{if } k_x = 0, \\ \frac{2\pi c_i(2c_i^2 + v_A^2)^{1/2}}{g} & \text{if } k_x \to \infty. \end{cases} \tag{A14}$$

Note that if the magnetic energy density is dominant over gas pressure, $\lambda_{\text{Parker}} \simeq 2\pi c_i v_A/g$. The wavelength λ_y for maximum growth occurs at

$$\lambda_{\max} = \begin{cases} \frac{2\pi(2c_i^2 + v_A^2)|v_A^2 - c_i^2|c_i^{1/2}}{g\{(c_i^2 + v_A^2)[2^{1/2}(c_i^2 + v_A^2)^{3/2} - c_i(c_i^2 + 3v_A^2)]\}^{1/2}} & \text{if } k_x = 0, \\ \frac{2\pi v_A^2(2c_i^2 + v_A^2)^{1/2}c_i^{1/2}}{g[2^{1/2}(2c_i^2 + v_A^2)^{3/2} - (4c_i^2 + 3v_A^2)c_i]^{1/2}} & \text{if } k_x \to \infty. \end{cases} \tag{A15}$$

In the limit of strong magnetic fields, $\lambda_{\max} \simeq 2\pi v_A(v_A c_i)^{1/2}/(2^{1/4}g)$. The corresponding maximum growth rate is

$$\gamma_{\max} = \begin{cases} \frac{g v_A(c_i^2 + v_A^2)^{1/2}[3c_i^2 + v_A^2 - 2^{3/2}(c_i^2 + v_A^2)^{1/2}c_i]^{1/2}}{(2c_i^2 + v_A^2)|v_A^2 - c_i^2|}. & \text{if } k_x = 0, \\ \frac{g[4c_i^2 + v_A^2 - 2^{3/2}(2c_i^2 + v_A^2)^{1/2}c_i]^{1/2}}{v_A(2c_i^2 + v_A^2)^{1/2}} & \text{if } k_x \to \infty. \end{cases} \tag{A16}$$

For strong magnetic fields, this becomes simply $\gamma_{\mathrm{max}} \simeq g/v_{\mathrm{A}}$.

REFERENCES

Agol, E., & Blaes, O. 1996, MNRAS, 282, 965

Agol, E., & Krolik, J. 1998, ApJ, 507, 304

Balbus, S. A., & Hawley, J. F. 1998, Rev. Mod. Phys., 70, 1

Ballantyne, D. R., Turner, N. J., & Blaes, O. M. 2004, ApJ, 603, 436

Ballantyne, D. R., Turner, N. J., & Young, A. J. 2005, ApJ, 619, 1028

Begelman, M. C. 2001, ApJ, 551, 897

Begelman, M. C. 2002, ApJ, 568, L97

Begelman, M. C. 2006, ApJ, 643, 1065

Blaes, O., & Socrates, A. 2003, ApJ, 596, 509

Blaes, O. M., Davis, S. W., Hirose, S., Krolik, J. H., & Stone, J. M. 2006, ApJ, 645, 1402

Brandenburg, A., Nordlund, Å., Stein, R.F. & Torkelsson, U. 1995, ApJ, 446, 741

Chandrasekhar, S. 1967, An Introduction to the Study of Stellar Structure (New York: Dover)

Coleman, H. H., & Shields, G. A. 1990, ApJ, 363, 415

Davis, S., Blaes, O., Turner, N., & Socrates, A. 2004, in ASP Conf. Ser. 311, AGN Physics with the Sloan Digital Sky Survey, ed. G. T. Richards & P. B. Hall (San Francisco: ASP), 135

Gammie, C.F. 1998, MNRAS, 297, 929

Gnedin, Yu. N., & Silant'ev, N. A. 1978, SvA, 22, 325

Hirose, S., Krolik, J. H., & Stone, J. M. 2006, ApJ, 640, 901

Kim, W.-T., & Ostriker, E. C. 2000, ApJ, 540, 372

Krolik, J. H. 1999, Active Galactic Nuclei (Princeton: Princeton Univ. Press)

Krolik, J. H., Hirose, S., & Blaes, O. 2007, ApJ, submitted

Lightman, A. P., & Eardley, D. M. 1974, ApJ, 187, L1

Mihalas, D., & Mihalas, B. W. 1984, Foundations of Radiation Hydrodynamics (New York: Oxford Univ. Press)

Miller, K. A., & Stone, J. M. 2000, ApJ, 534, 398

Nayakshin, S., Kazanas, D., & Kallman, T. R. 2000, ApJ, 537, 833

Novikov, I. D., & Thorne, K. S. 1973, in Black Holes, ed. C. DeWitt & B. S. DeWitt (New York: Gordon & Breach), 343

Nowak, M. A., & Wagoner, R. V. 1993, ApJ, 418, 187

Parker, E. N. 1966, ApJ, 145, 811

Parker, E. N. 1967, ApJ, 149, 535

Pessah, M. E., & Psaltis, D. 2005, ApJ, 628, 879

Shakura, N.I. & Sunyaev, R.A. 1973, A&A, 24, 337

Shakura, N. I., & Sunyaev, R. A. 1976, MNRAS, 175, 613

Stone, J. M., Hawley, J. F., Gammie, C. F., & Balbus, S. A. 1996, ApJ, 463, 656

Turner, N. J., 2004, ApJ, 605, L45

Turner, N. J., Blaes, O. M., Socrates, A., Begelman, M. C., & Davis, S. W. 2005, ApJ, 624, 267
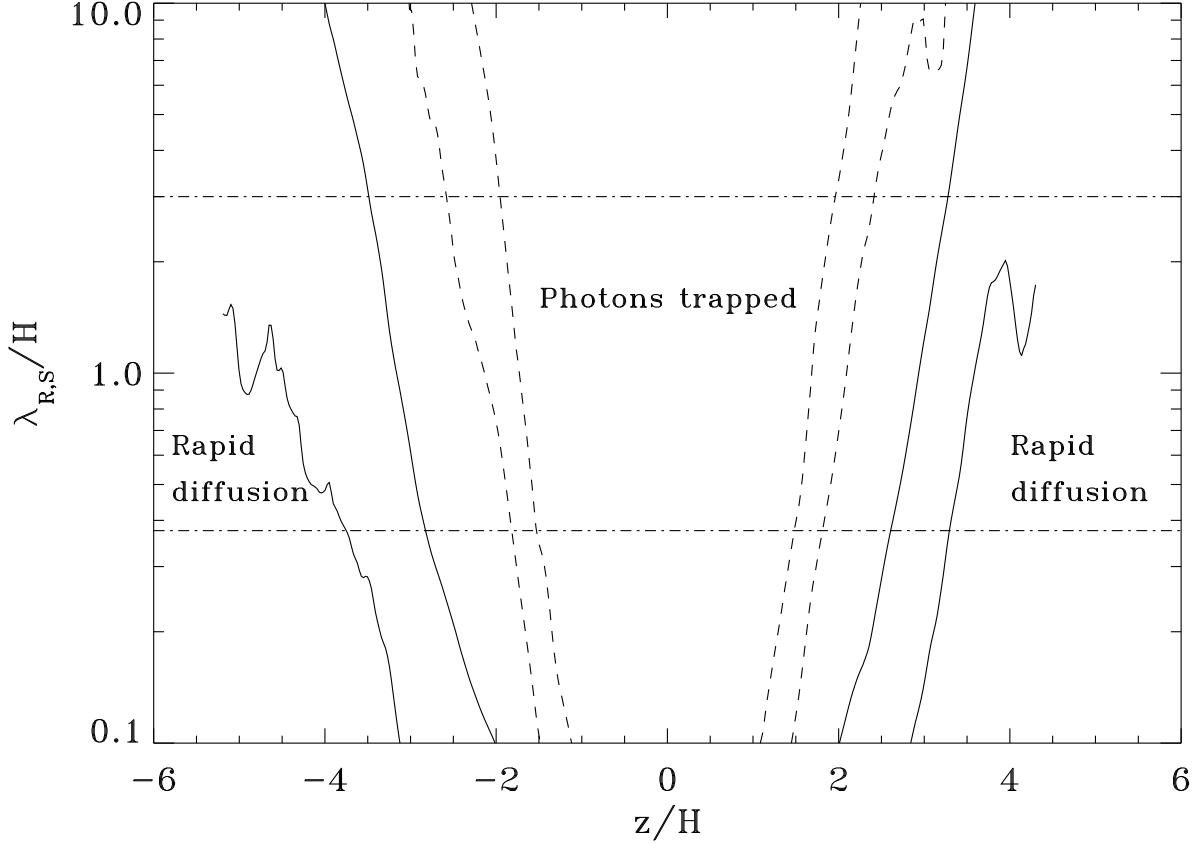
Fig. 1.— Wavelength λ_R below which rapid photon diffusion applies (lower of each pair of curves), and wavelength λ_S above which photons are trapped (upper of each pair of curves) for acoustic disturbances in the simulation. The solid and dashed pair of curves correspond to horizontally averaged conditions at the highest ($t = 90$ orbits) and lowest ($t = 150$ orbits) total energy epochs, respectively. The curves extend only out to the Rosseland mean photosphere of the horizontally averaged structure in each case, outside of which photon diffusion does not apply. For comparison, the lower horizontal dot-dashed line shows the length $8r\Delta\phi$ of eight grid zones in the azimuthal direction, close to the minimum wavelength that the code can resolve. The upper horizontal dot-dashed line shows the length $3H$ of the box in the azimuthal direction.
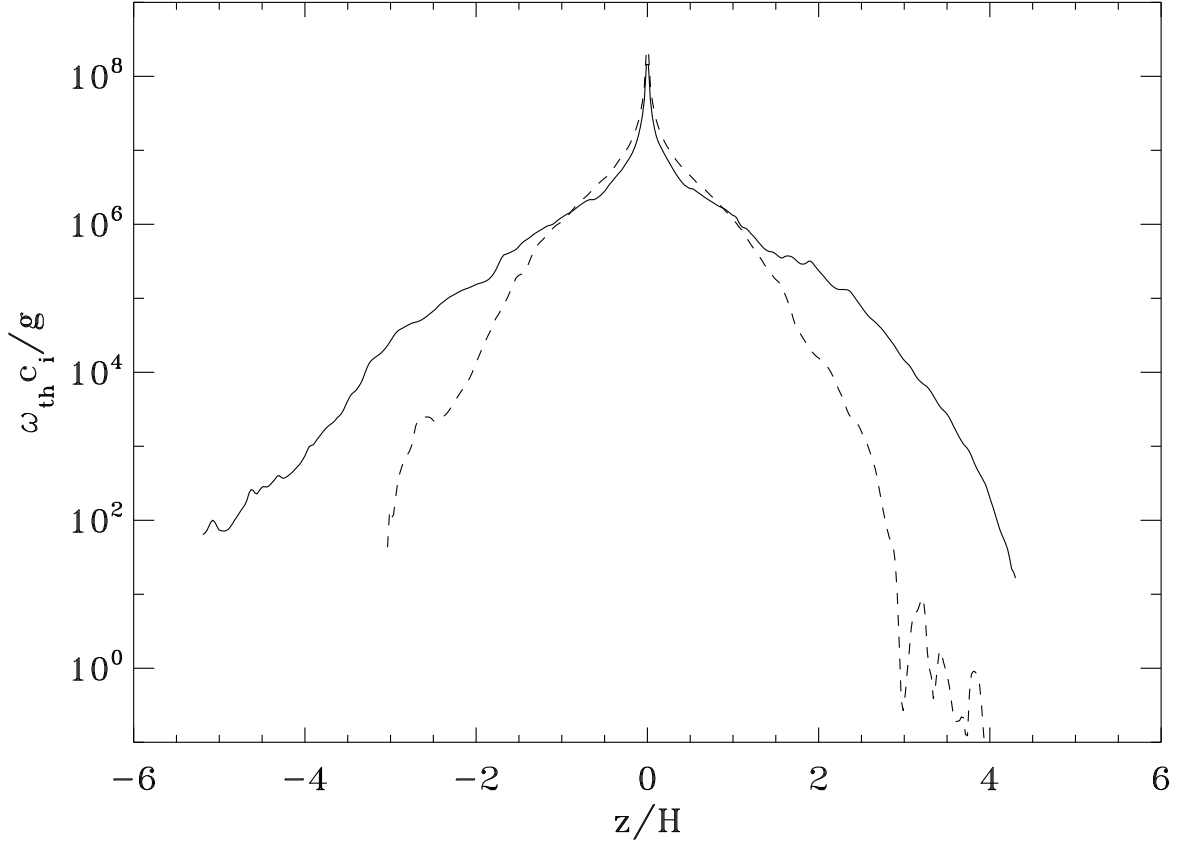
Fig. 2.— Scaled photon/gas thermal coupling frequency calculated from the horizontally averaged structure at $t = 90$ orbits (solid) and $t = 150$ orbits (dashed). Tight thermal coupling is a good approximation for photon bubbles if this scaled frequency is much greater than unity.
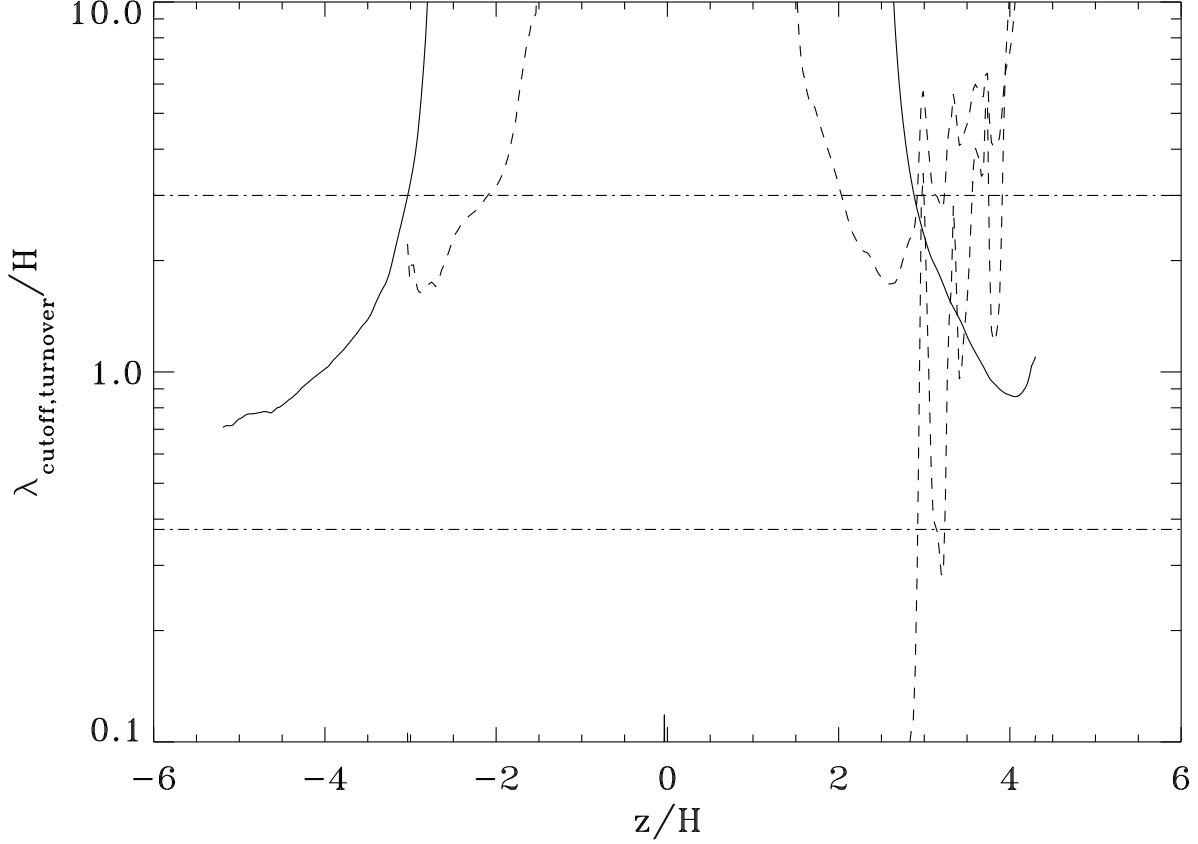
Fig. 3.— Range of wavelengths over which the asymptotic photon bubble growth rates of Fig. 4 should be valid (provided these wavelengths are also in the rapid photon diffusion regime), as a function of height in the box at $t = 90$ orbits (solid) and $t = 150$ orbits (dashed). The solid and upper dashed curves in each epoch correspond to the turnover wavelength, while the lower dashed curve on the right corresponds to the thermal cutoff wavelength at $t = 150$ orbits. (The thermal cutoff wavelength for $t = 90$ orbits is less than $0.1H$ at all heights, and is also less than $0.1H$ for $z < 2.8H$ at $t = 150$ orbits.) Rapid growth rates should exist between the thermal cutoff and turnover wavelengths. The lower and upper horizontal dashed lines again indicate eight cell sizes $8r\Delta\phi$ and the length $3H$ of the box in the azimuthal direction, respectively.
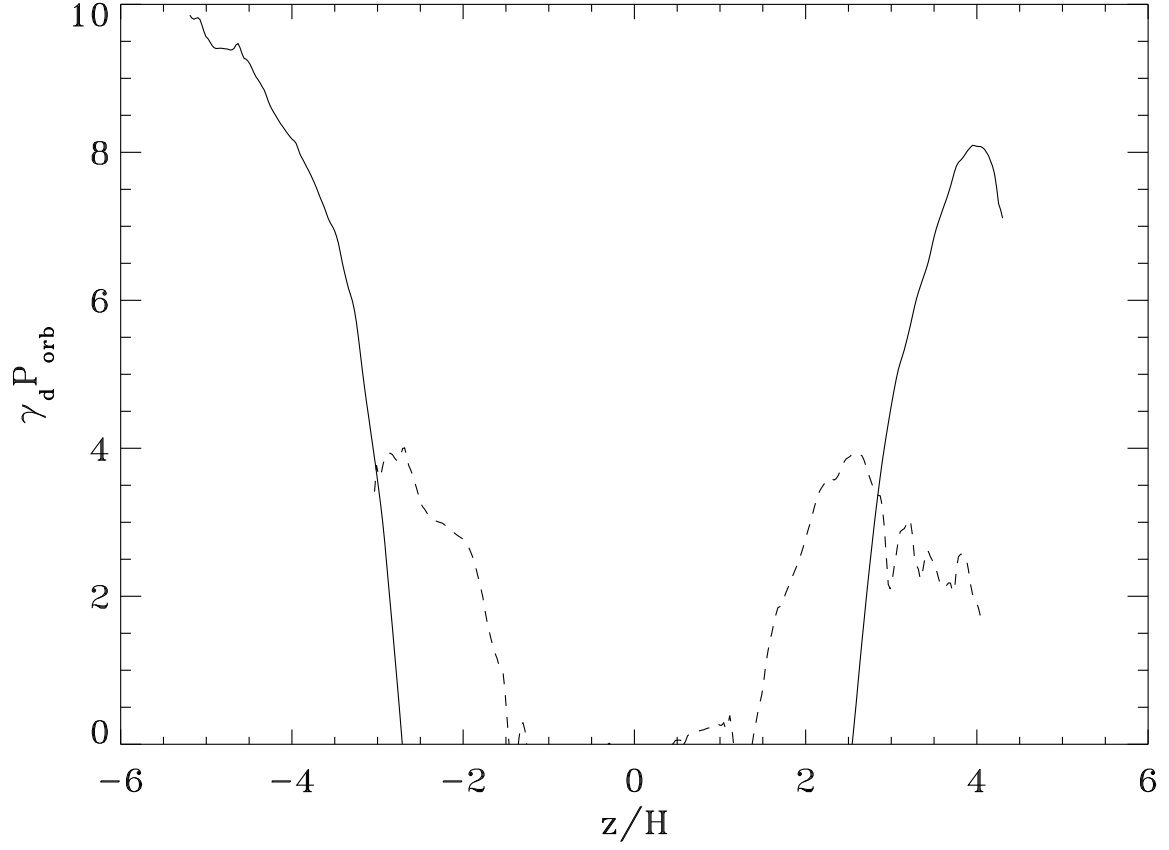
Fig. 4.— Short wavelength photon bubble growth rate γ_d scaled with the orbital period $P_{\mathrm{orb}} = 2\pi/\Omega$, as a function of height at $t = 90$ orbits (solid) and $t = 150$ orbits (dashed). Growth rates are shown only at heights deeper than the photosphere of the horizontally averaged structure at that epoch.
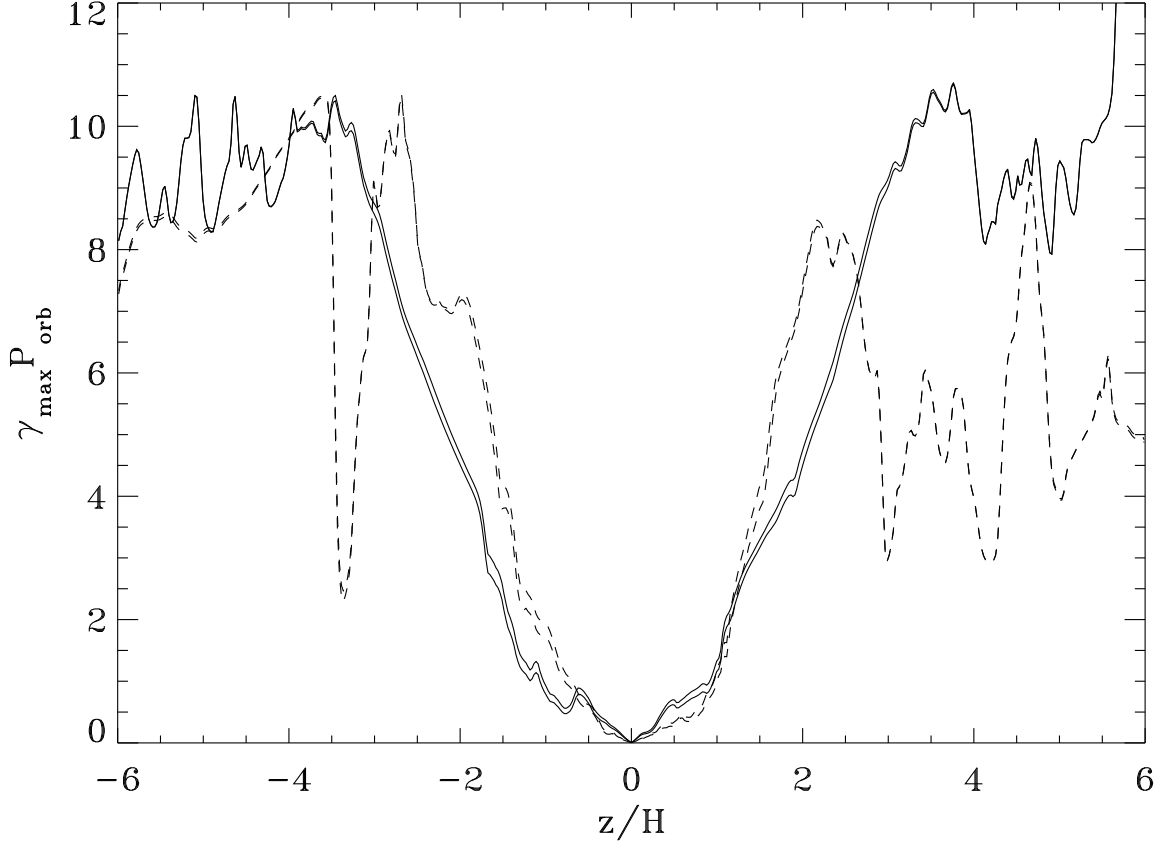
Fig. 5.— Maximum Parker instability growth rate γ_{max} from equation (A16), scaled with the orbital period $P_{orb} = 2\pi/\Omega$, as a function of height in the box at $t = 90$ orbits (solid) and $t = 150$ orbits (dashed). The two nearly identical curves for each epoch correspond to the $k_x = 0$ and ∞ limits.
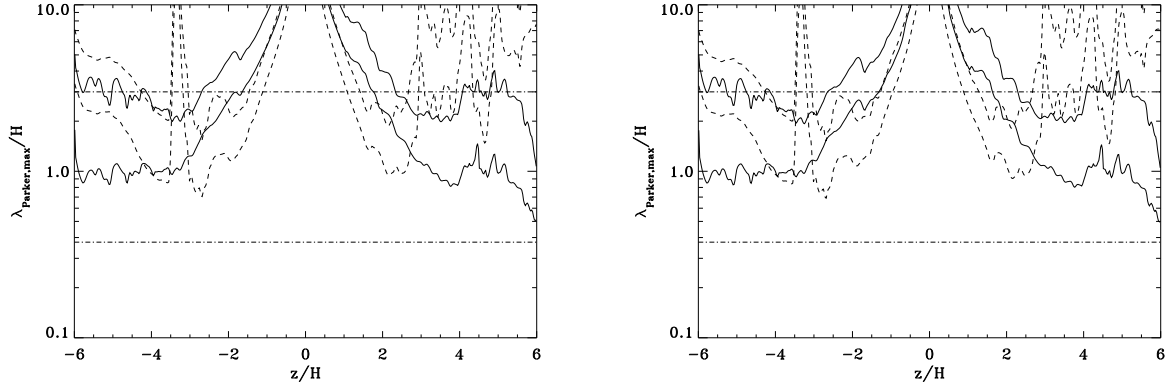
Fig. 6.— Minimum Parker instability wavelength from equation (A14) (lower of each pair of curves) and wavelength for maximal Parker growth rate from equation (A15) (upper of each pair of curves) as a function of height in the box at $t = 90$ orbits (solid curve pair) and $t = 150$ orbits (dashed curve pair). Eight cell sizes and the length of the box in the azimuthal direction are indicated again by the lower and upper horizontal dashed lines, respectively. The left hand panel corresponds to $k_x = 0$, while the right hand panel corresponds to $k_x \to \infty$. The dependence on k_x is very weak.
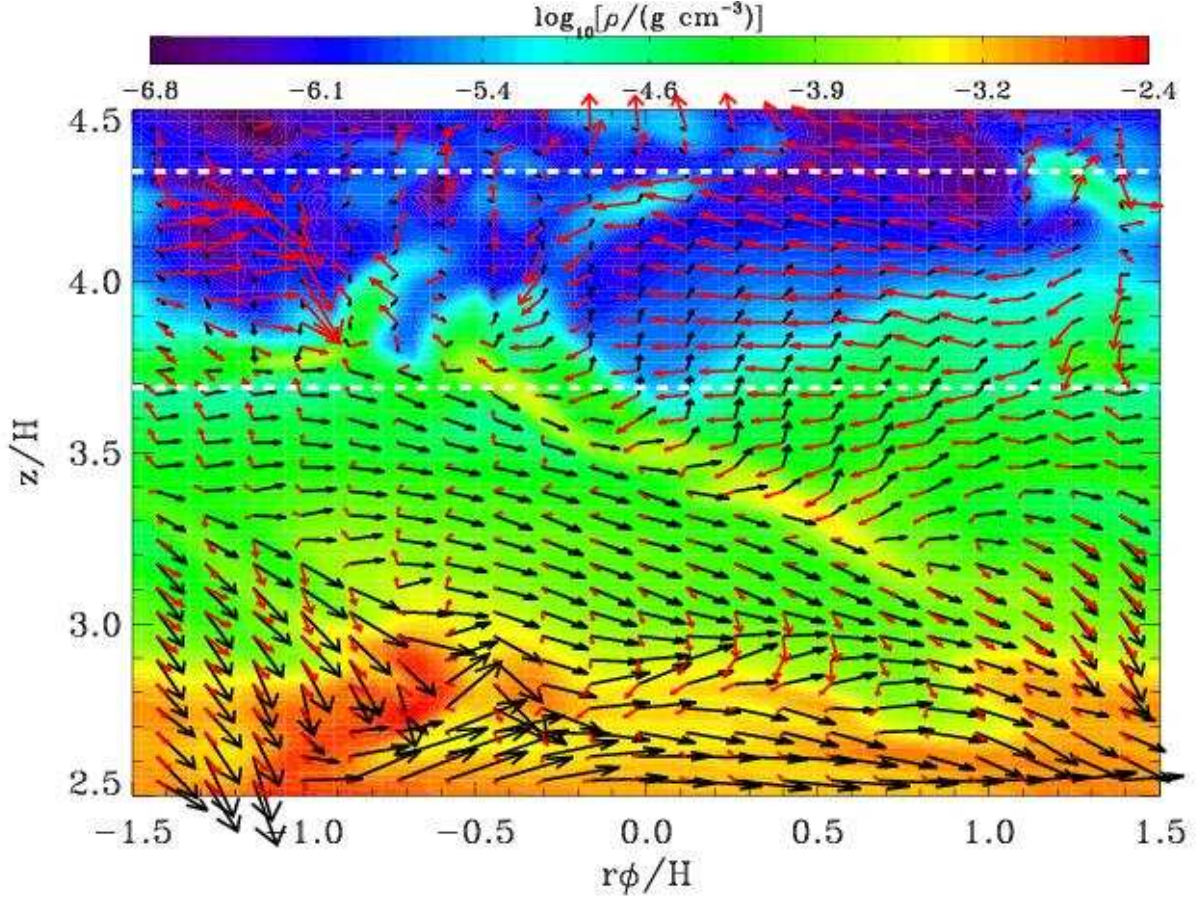
Fig. 7.— Density in regions under the horizontally-averaged upper photosphere (dashed line) in a fixed radial slice near the middle of the box at $t = 90$ orbits. The arrows show the projections of magnetic field vectors (black) and velocity vectors relative to the background shear flow (red) in this radial slice, computed at the position of the tail of each arrow. Horizontal dashed lines indicate the positions of the Rosseland mean photosphere (upper) and effective photosphere (lower), computed from the horizontally averaged structure.
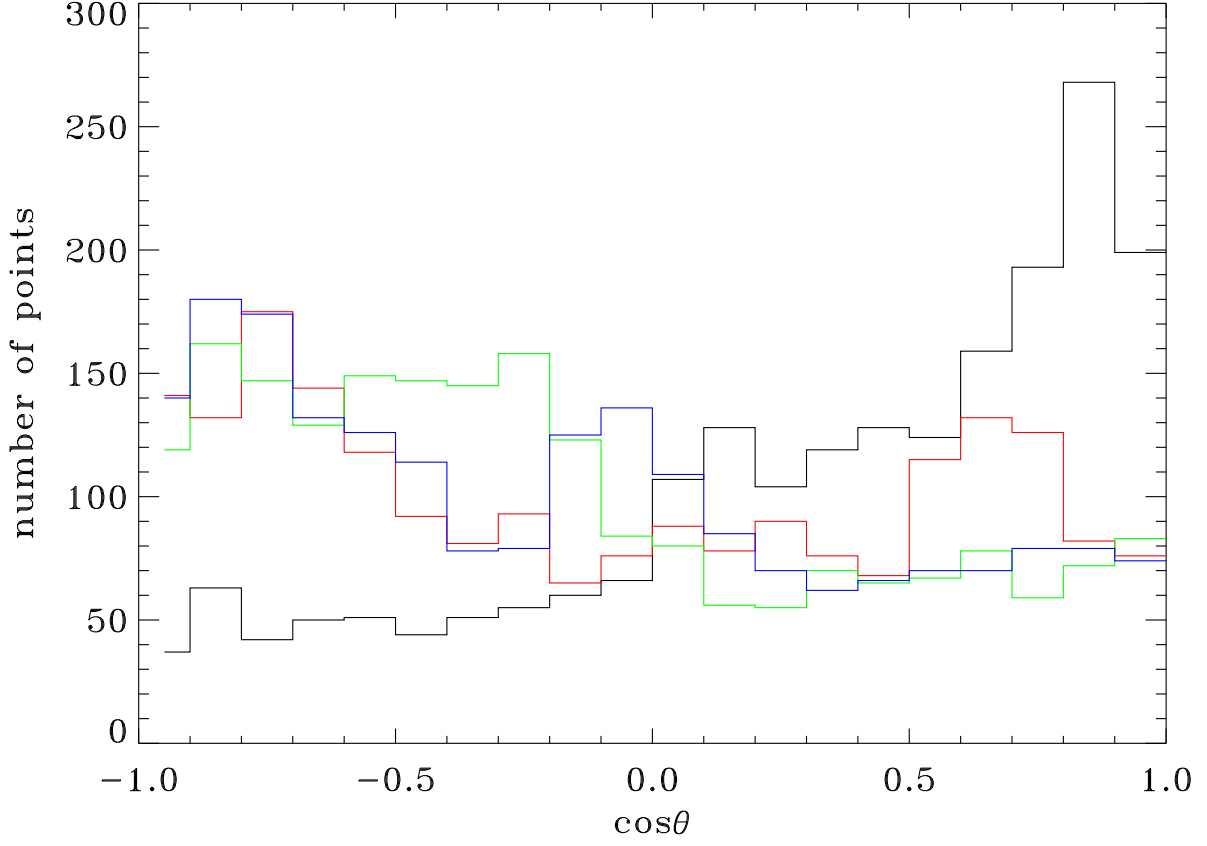
Fig. 8.— Distribution of cosines of the angle θ between the perturbed radiation flux vector and the fluid velocity relative to the background shear flow, over horizontal slices in the simulation at $t = 90$ orbits. Different histograms correspond to different heights: $+2.4H$ (black), $+2.9H$ (red), $+3.3H$ (green), and $+3.8H$ (blue).
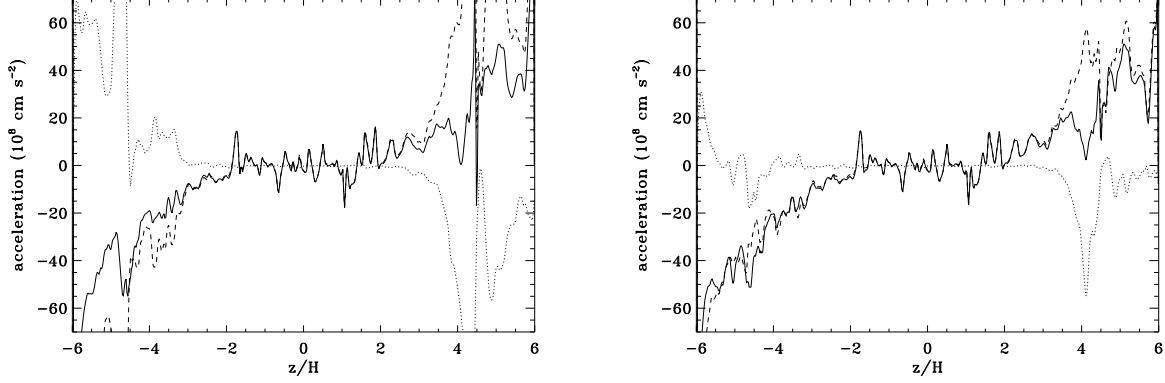
Fig. 9.— Spatially horizontally averaged (left) and mass-weighted horizontally averaged (right) contributions to the outward vertical accelerations from magnetic pressure gradients (dashed) and magnetic tension (dotted), at $t = 90$ orbits. The solid curves show the sum of these magnetic accelerations.
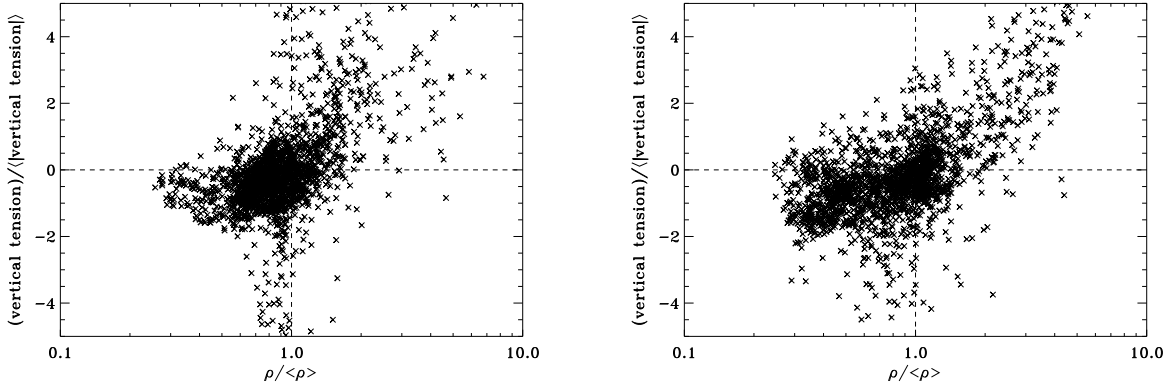
Fig. 10.— Vertical magnetic tension force per unit volume vs. density at each grid zone in a $z = 2.75H$ horizontal slice through the simulation at $t = 90$ orbits (left) and in a $z = 2H$ horizontal slice through the simulation at $t = 150$ orbits (right). The tension has been scaled by the average magnitude of the tension force in this horizontal slice, and the density has been scaled by the average density.
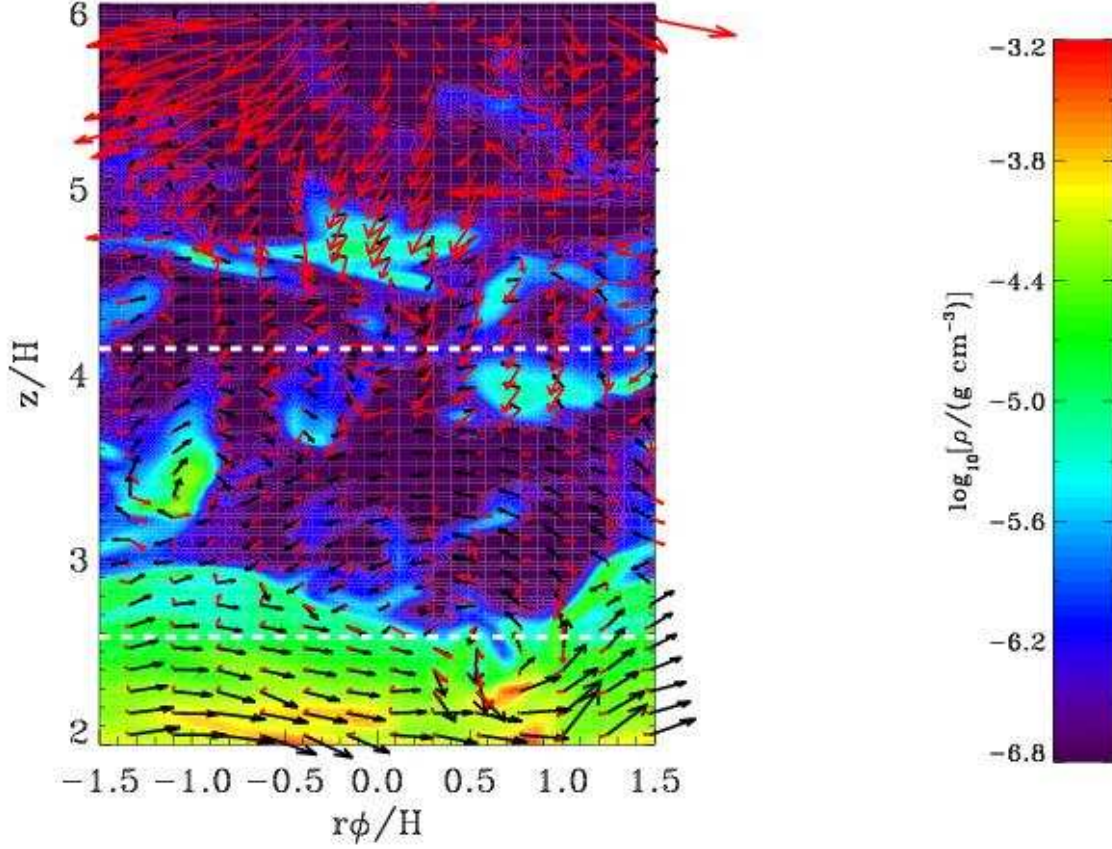
Fig. 11.— Density in the upper layers ($2H < z < 6H$) in a fixed radial slice near the middle of the box at time 150 orbits. The arrows show the projections of magnetic field vectors (black) and velocity vectors relative to the background shear flow (red) into this radial slice, computed at the position of the tail of each arrow. The Rosseland mean and effective photospheres of the horizontally averaged structure at this time are indicated by the upper and lower dashed lines, respectively.
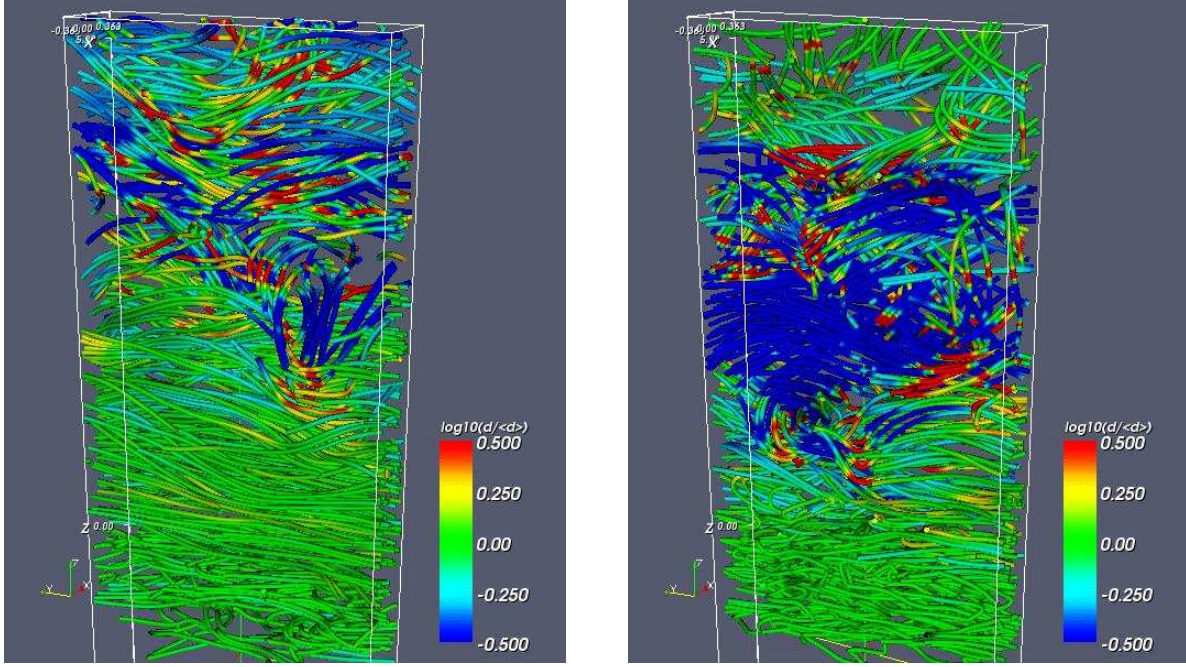
Fig. 12.— Magnetic field lines in the simulation domain at 90 orbits (left) and 150 orbits (right). The lines are color coded with the local fluid density scaled by the horizontally averaged density at the same height.
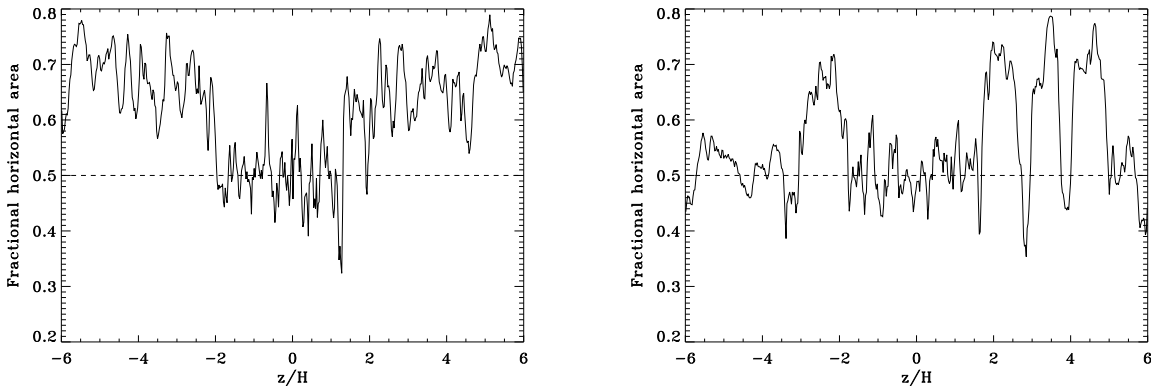
Fig. 13.— The fractional horizontal area over which higher (lower) than average densities are associated with vertically inward (outward) magnetic tension forces, as a function of height in the simulation. The left panel is for $t = 90$ orbits and the right panel is for $t = 150$ orbits.
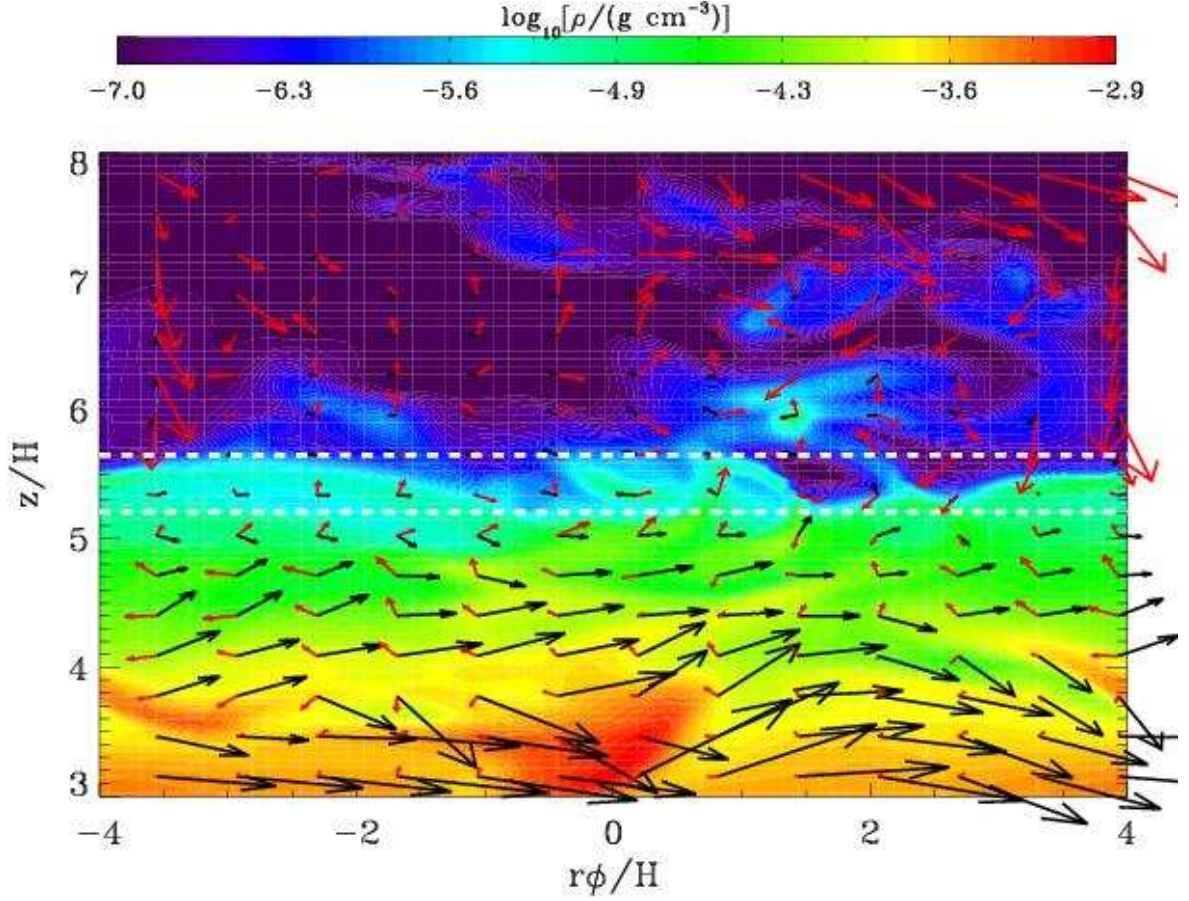
Fig. 14.— Density in the uppermost surface layers $(3H < z < 8H)$ in a fixed radial slice near the middle of the box at time 60 orbits from the gas pressure dominated simulation of Hirose, Krolik, & Stone (2006). The arrows show the projections of magnetic field vectors (black) and velocity vectors relative to the background shear flow (red) into this radial slice, computed at the position of the tail of each arrow. The Rosseland mean and effective photospheres of the horizontally averaged structure at this time are indicated by the upper and lower dashed lines, respectively.
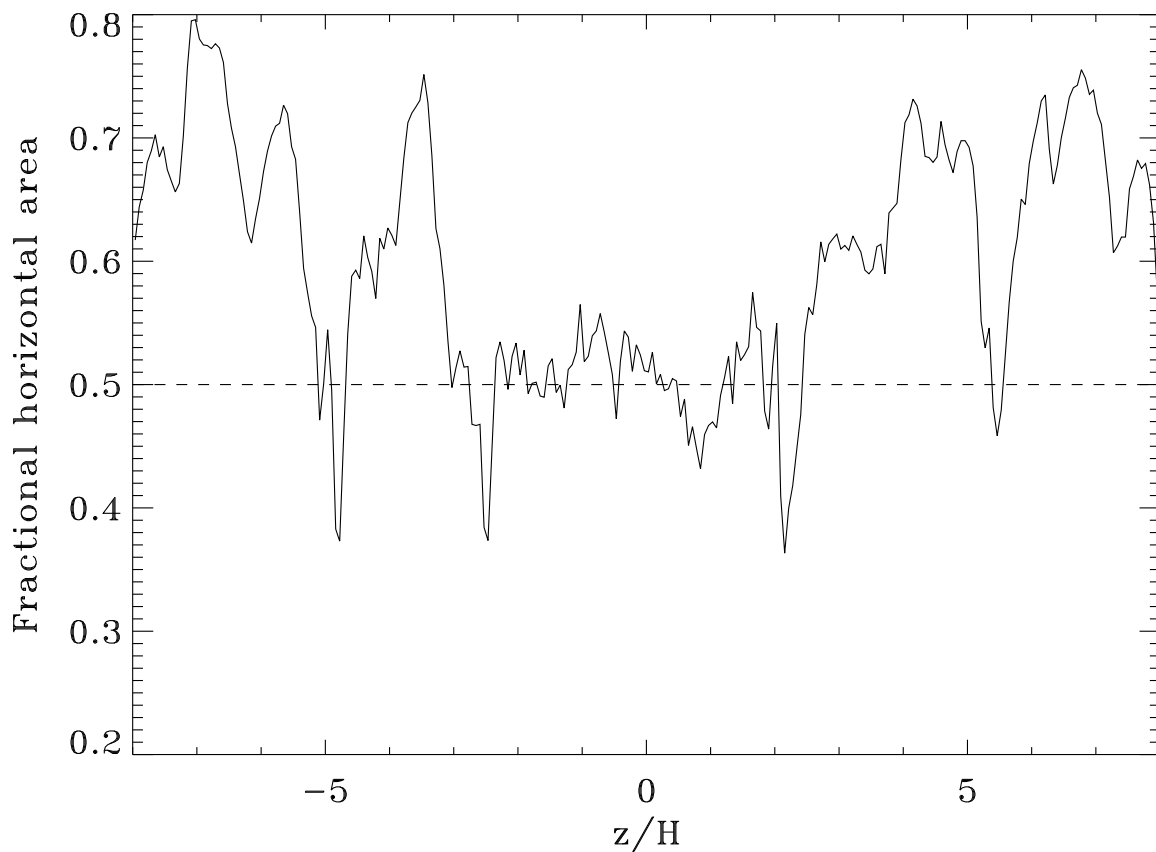
Fig. 15.— Same as Fig. 13 except for the gas pressure dominated simulation of Hirose, Krolik, & Stone (2006) at time 60 orbits.
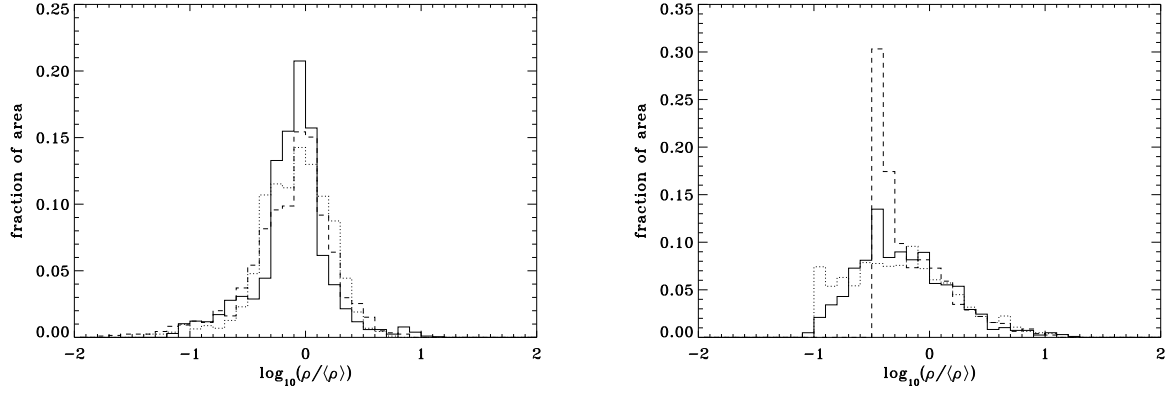
Fig. 16.— Distribution of densities, scaled with the horizontally averaged density, at the heights of the upper effective (left) and Rosseland mean (right) photospheres at 90 orbits (solid histograms) and 150 orbits (dashed histograms). For comparison, the dotted histograms show the corresponding density distributions in the gas pressure dominated simulation of Hirose, Krolik, & Stone (2006) at 60 orbits.
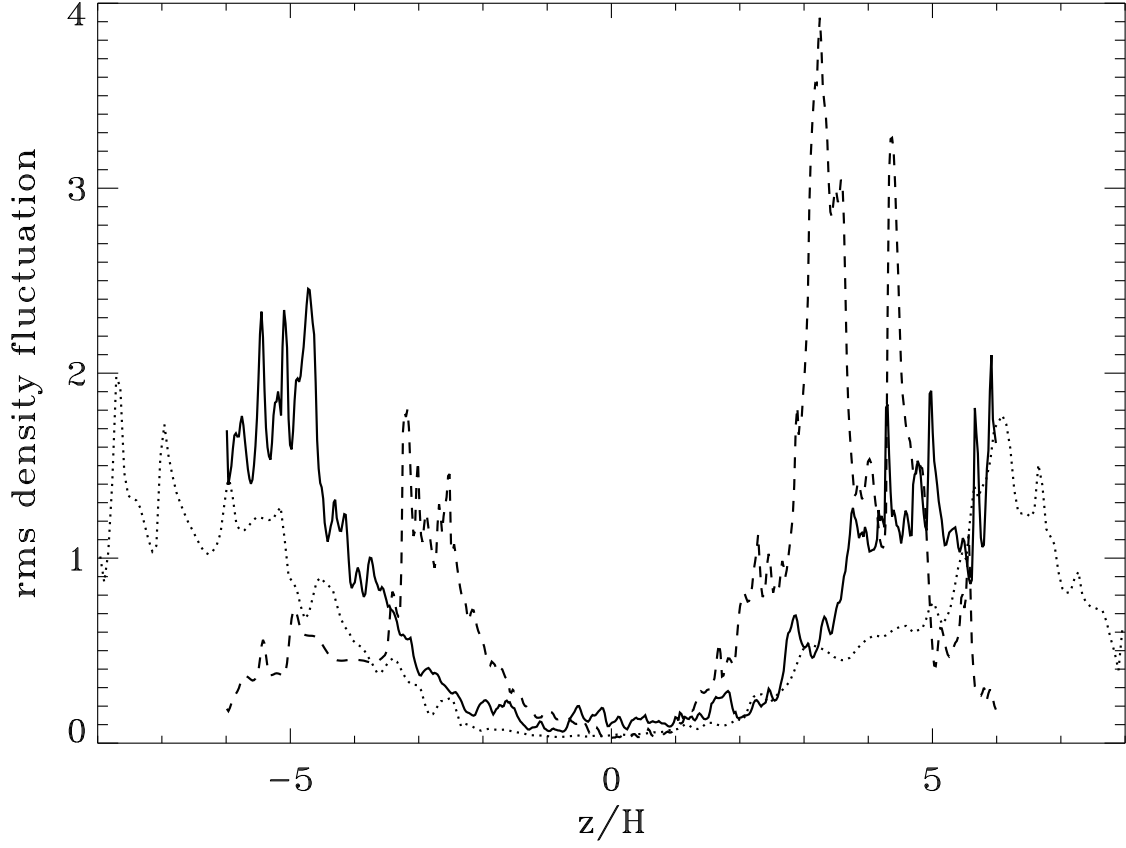
Fig. 17.— Root mean square fractional fluctuation of density as a function of height at 90 orbits (solid) and 150 orbits (dashed). For comparison, the dotted curve shows the same thing in the gas pressure dominated simulation of Hirose, Krolik, & Stone (2006) at 60 orbits.
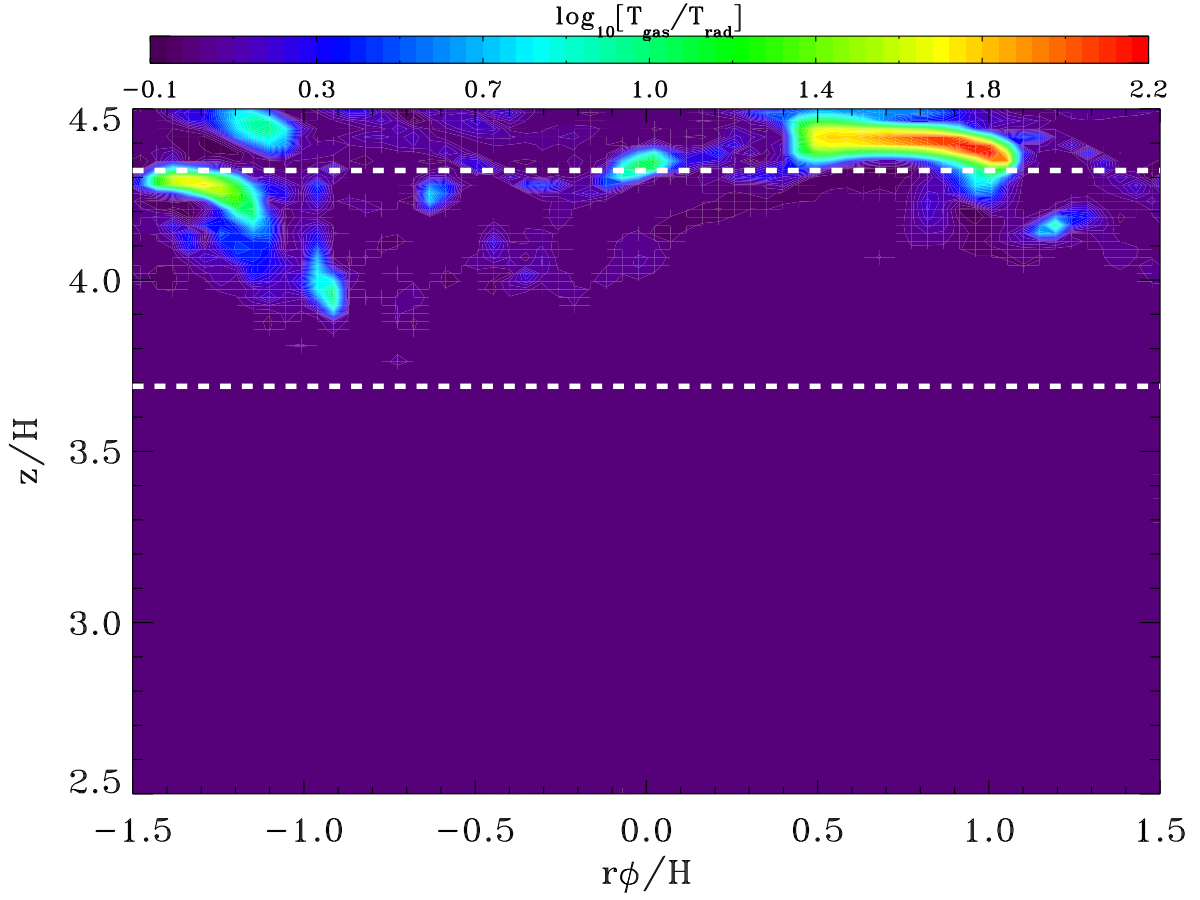
Fig. 18.— Ratio of gas to radiation temperature near the upper photosphere in a fixed radial slice near the middle of the box at t=90 orbits. (The radial slice is identical to that chosen in Fig. 7.) Horizontal dashed lines indicate the positions of the Rosseland mean photosphere (upper) and effective photosphere (lower), computed from the horizontally averaged structure.
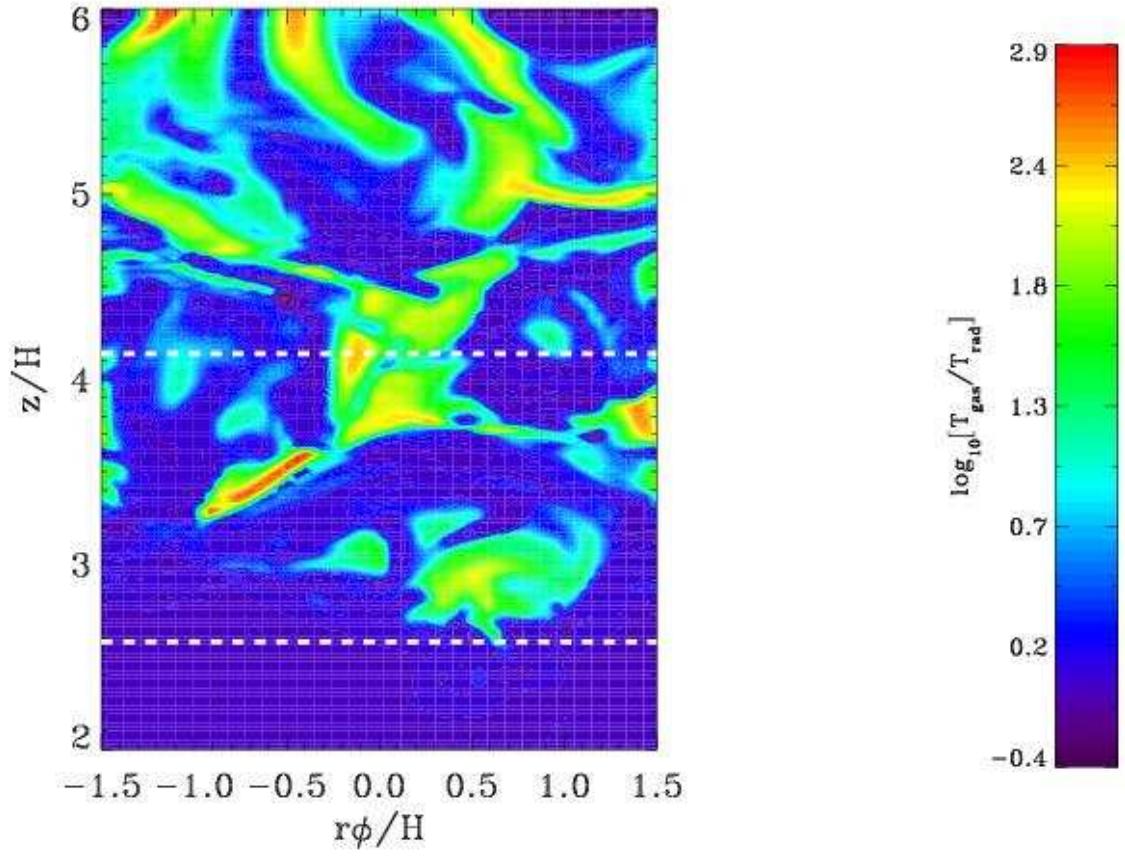
Fig. 19.— Same as Fig. 18 except at t=150 orbits. (The corresponding density structure is shown in Fig. 11.)